Journal of Rock Mechanics and Geotechnical Engineering 16 (2024) 682–696

Contents lists available at ScienceDirect

Journal of Rock Mechanics and Geotechnical Engineering

journal homepage: www.jrmge.cn

Full Length Article

Numerical analysis of geosynthetic-reinforced embankment performance under moving loads

Xuanming Ding [a], Jinqiao Zhao [a,b], Qiang Ou [a,*], Jianfei Liu [c]

[a] College of Civil Engineering, Chongqing University, Chongqing, 400045, China
[b] Key Laboratory of New Technology for Construction of Cities in Mountain Area, Chongqing University, Chongqing, 400045, China
[c] China United Engineering Corporation Limited, Hangzhou, 310052, China

ARTICLE INFO

Article history:
Received 30 November 2022
Received in revised form
22 March 2023
Accepted 12 April 2023
Available online 15 July 2023

Keywords:
Geosynthetic-reinforced layer
Numerical model
Moving load
Embankment
Deformation
Stress

ABSTRACT

The performance of geosynthetic-reinforced embankments under traffic moving loads is always a hot-spot in the geotechnical engineering field. A three-dimensional (3D) model of a geosynthetic-reinforced embankment without drainage consolidation was established using the finite element software ABAQUS. In this model, the traffic loads were simulated by two moving loads of rectangular pattern, and their amplitude, range, and moving speed were realized by a Fortran subroutine. The embankment fill was simulated by an equivalent linear viscoelastic model, which can reflect its viscoelasticity. The geogrid was simulated by the truss element, and the geocell was simulated by the membrane element. Infinite elements were utilized to weaken the boundary effect caused by the model geometry at the boundaries. Validation of the established numerical model was conducted by comparing the predicted deformations in the cross-section of the geosynthetic-reinforced embankment with those from the existing literature. On this basis, the dynamic stress and strain distribution in the pavement structure layer of the geosynthetic-reinforced embankment under a moving load was also analyzed. Finally, a parametric study was conducted to examine the influences of the different types of reinforcement, overload, and the moving load velocity on the geosynthetic-reinforced embankment.

1. Introduction

Geosynthetic (e.g. geogrid or geocell)-reinforced mattresses have been widely used in geotechnical engineering, including slopes, highway embankments, and soft foundations, especially those with strict requirements for rapid construction and small settlement (Abdullah and Edil, 2007; Deb et al., 2007, 2011; Zhang et al., 2010; Dash and Bora, 2013; Hong and Wu, 2013; Liu et al., 2023). Among them, geosynthetic-reinforced embankment system is one of the most popular applications, even though it is relatively complicated. Numerous studies have been performed on this subject utilizing different means, such as field investigations, laboratory tests, analytical methods, and numerical simulations (Zhang et al., 2018, 2020; Zhou et al., 2018; Zhuang et al., 2020). Over the past decades, numerous laboratory studies have been conducted to understand the performance of geosynthetic-reinforced soil under static loading (Dash, 2003, 2012; Leshchinsky and Ling, 2013; Peng et al., 2021; Zhuang et al., 2022), and moving loads (Indraratna et al., 2015; Biabani et al., 2016; Biswas et al., 2016; Dutta and Mandal, 2016; Ngo et al., 2016; Suku et al., 2016; Thakur et al., 2017). However, the former three methods may not be capable of considering all the aspects involved, such as the boundary, scale, and time lag effects. To this end, numerical simulation has been adopted as an ideal alternative (Maheshwari et al., 2004; Bourgeois et al., 2011; Huang et al., 2011; Thach et al., 2013; Hegde and Sitharam, 2015; Qian et al., 2015; Shi et al., 2016; Tang et al., 2016; Chen and Zhou, 2018; Zhang et al., 2022), and it may be applicable to the most engineering problems with effectiveness.

Fakher and Jones (2001) numerically investigated a layer of sand overlaying a layer of geosynthetic reinforcement and super soft clay, and the factors affecting the reinforcement mechanisms of the geosynthetic reinforcement in super soft clay were considered. Hegde and Sitharam (2015) presented a realistic modeling approach to simulate the geocells in a three-dimensional (3D) framework. It was found that the geocells could transfer part of the

* Corresponding author.
E-mail address: ouq126@cqu.edu.cn (Q. Ou).
Peer review under responsibility of Institute of Rock and Soil Mechanics, Chinese Academy of Sciences.

https://doi.org/10.1016/j.jrmge.2023.04.019

vertical loading to the lateral direction compared with the unreinforced case and the geogrid-reinforced case. Shadi et al. (2019) investigated the effect of the reinforcement geometrical parameters on the bearing capacity of the foundation soil through PLAXIS-3D. The results showed that the bearing capacity increased when reinforced with a geotextile reinforcement using the wraparound reinforcement technique. Han and Gabr (2002) numerically investigated pile–soil–geosynthetics interactions by considering three major influence factors, i.e. height of the fill, tensile stiffness of the geosynthetic, and elastic modulus of the pile material.

In addition, a geotextile-reinforced embankment may not always just bear the static load. Nevertheless, the nonstatic load may exist in some cases. Biabani et al. (2016) conducted a series of 3D numerical simulations in ABAQUS to analyze realistically cellular confinement subjected to cyclic loading. The results showed that the geocell could effectively decrease the lateral and axial deformations of the reinforced subballast. Pham and Dias (2019) investigated the behavior of pile-supported embankments subjected to different traffic cyclic loadings. The influences of the traffic load cycles, vehicle speed, and embankment height on the arching effect and the cumulative settlement were investigated.

Although several studies on the geosynthetic-reinforced embankment have been reported in the recent years, numerical simulations are mainly focused on static load. The moving traffic load was frequently treated as a concentrated load or a strip load in most previous studies. However, the traffic load may be time-dependent in practice. Therefore, it remains an open question to realize the characteristic of the moving traffic load when conducting finite element analysis. To the best of the authors' knowledge, few studies have simultaneously taken viscoelastic model and the geosynthetic–soil interaction into consideration.

In this context, an approach is proposed to model geosynthetics in a 3D framework, and the performance of the geosynthetic-reinforced embankment under a moving load in ABAQUS is predicted. This approach can consider the viscoelastic constitutive model and controllable moving loads. Meanwhile, the infinite element is utilized to reduce the boundary effect induced by model size at the boundaries. In addition, the coupling effect between the different layers in the embankment is taken into account to assess the responses of the upper and lower parts.

2. Numerical model

To analyze the performance of geosynthetic-reinforced embankment under a moving load, a 3D numerical model was established using the finite element software ABAQUS. It is assumed that the initial ground stress of the foundation is composed of the vertical gravity stress of the soil, and only the increase in gravitational stress is considered during embankment filling.

2.1. Geometric size and parameters

A typical geosynthetic-reinforced embankment under moving loads is adopted in this study. Fig. 1 shows the profile of the longitudinal section of the geosynthetic-reinforced embankment. As the aim of this study is focusing on low embankment, the effective height of the embankment fill is generally no more than 3 m, and h_2 generally has a value 0.3–0.5 m. Fig. 2 presents the profile of the cross-section of the geosynthetic-reinforced embankment. A 3D numerical model is set up as portrayed in Fig. 3. The geometric parameters of the model are presented in Table 1.

The parameters of the foundation soil, embankment fill, and geosynthetic-reinforced materials were selected according to those in the literature (Zhang et al. 2018, 2020). A geogrid was adopted as

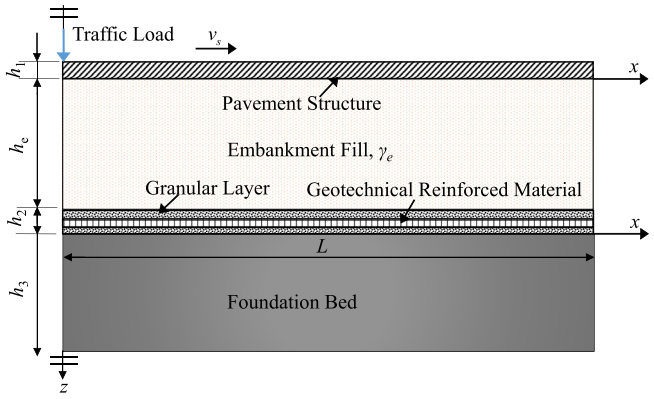

Fig. 1. The profile of the longitudinal section of the geosynthetic-reinforced embankment. V_s is the velocity of the moving load. h_1 is the height of the pavement structure layer and h_e is the effective height of the embankment fill. h_2 is the height of the reinforced cushion layer, including the gravel cushion layer and geosynthetic-reinforced materials. h_3 is the height of the substratum of the foundation, considering the boundary effect and the calculation efficiency of the numerical model, and $h_3 = (2–3)h_e$ in this study. L is the length in longitudinal direction of the geosynthetic-reinforced embankment, and $L = 20$ m in the numerical simulation.

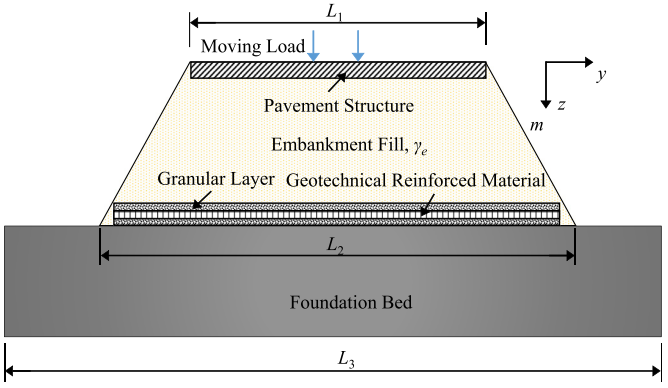

Fig. 2. The profile of the cross-section of the geosynthetic-reinforced embankment. L_1 is the width of the pavement structure layer, and the basic width is calculated based on a two-way two-lane scheme with $L_1 = 10$ m. L_2 is the width at the bottom of the geosynthetic-reinforced embankment (i.e. the width of the reinforced cushion layer). m is the slope ratio of the reinforced embankment; and L_3 is the width of the foundation soil.

the reinforcement material, with rupture elongation less than 4% and rupture strength higher than 50 kN/m. The linear elastic model was used for the geogrid, and the detailed parameters are summarized in Table 2. The parameters for the geocell are listed in Table 3. Considering the viscoelasticity of the embankment fill and foundation soil, the parameters of the pavement structure layer, embankment fill and foundation soil are tabulated in Table 4.

2.2. Initial and boundary conditions

The in situ stress equilibrium state before the embankment filling was taken into consideration as the initial condition. The stress equilibrium state was achieved by numerical modeling of the gravitational loading and the manually applied reverse body forces. Only the superposition of gravity in the layered filling of the geosynthetic-reinforced embankment was taken into account, while the consolidation effect was not considered in this study. In addition, the initial stress that already existed in the embankment

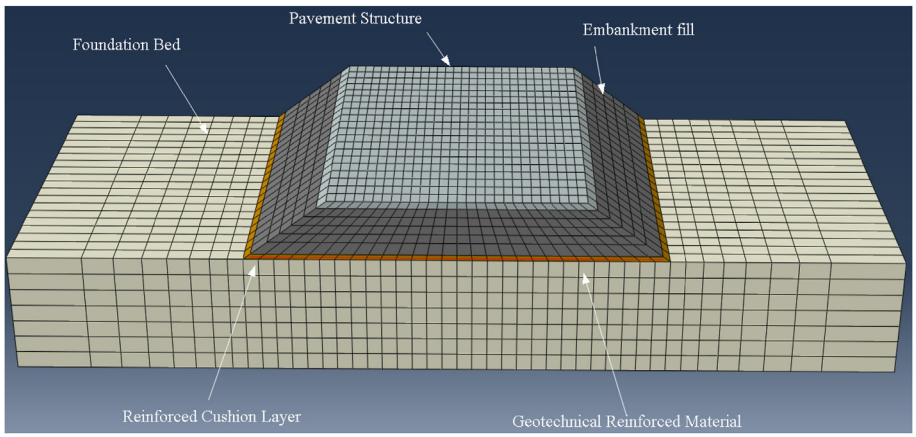

Fig. 3. The 3D numerical model of the geosynthetic-reinforced embankment.

before the external load was applied to the top surface of the geosynthetic-reinforced embankment.

To investigate the performance of the geosynthetic-reinforced embankment under moving loads, the model boundary conditions were defined as follows: (1) the displacements in all directions across the bottom boundary were restrained; (2) the front and rear sections along the embankment axis line (including the foundation soil, reinforced cushion layer, embankment fill, and pavement structure layer) constrained the horizontal displacement U_1; and (3) the section at the far end of the reinforced embankment slope, which is mainly composed of soil, constrained the horizontal displacement U_2.

In geotechnical engineering, the actual foundation is a half-infinite space, thus the analysis area should be infinite. Boundaryless problems are often encountered in stress analysis, or the area of concern is small compared with the surrounding medium. Unbounded or infinite medium can be approximated by extending the finite element mesh to great distances. This method is not always reliable. Dynamic analysis is of particular concern when the grid may reflect energy back to the model built. ABAQUS provides a new method, where a half-infinite region can be defined using a selected appropriate attenuation function in the finite element modeling. This means that an infinite element is set at a certain distance from the target region, which can be flexibly connected with the finite element to simulate the infinite region. Here, the infinite element model based on solid elements was mainly used.

2.3. Element types and grids

The C3D8 solid element, i.e. the 8-node hexahedral linear solid element, was used to divide the pavement structure layer, embankment fill, and foundation soil. Considering that the main influence range of the moving load is the pavement structure layer and the upper half of the embankment fill, the changes in the stress and displacement are relatively obvious in this area. To ensure the accuracy and efficiency of the calculation results, the mesh of the pavement structure layer and the adjacent areas was divided denser, and the grid division of the foundation soil and distant areas was relatively sparse. Because the stress and deformation of the upper and lower surfaces need to be observed, the mesh is refined at the reinforced cushion layer. Meanwhile, the infinite element was used for both ends of the foundation soil. The model grid is shown in Fig. 4.

The geogrid is a network structure made up of two-dimensional (2D) line elements. The T3D2 truss element, i.e. the 2-node linear 3D truss element, was used to divide the geogrid elements. Considering the computation efficiency, the layout density of the grid was determined by the mesh size of the grid. The partitioning technique was structured, and the grid partition is shown in Fig. 5a. The geocell is a 3D spatial network structure consisting of 3D membrane elements, and the M3D4 quadrilateral linear element was used to divide the geocell elements. The partition is shown in Fig. 5b.

2.4. User-defined material mechanical behavior (UMAT) subroutine

The numerical simulation provides users with numerous unit libraries and material models (i.e. metal, rubber, plastic, concrete, and geosynthetics) that enable users to deal with a majority of problems. However, the common material models in the upper road engineering design (including the geosynthetic-reinforced materials and gravel cushion layer) are not included in the numerical simulation software. The UMAT is a user subroutine interface provided by the software for the secondary development of the material constitutive model. It can define all types of material constitutive models not available in the material library, which greatly enhances the application and flexibility of numerical simulation.

The ABAQUS main program and UMAT subroutine provide a dynamic interaction between the data transfer and the collaborative work process. The interaction calculation process between the main program and UMAT subroutine is as follows: from the moment t_n, the main program generates an external loading-induced strain increment $\Delta\varepsilon$ at Δt, and the UMAT subroutine provides a new Cauchy stress tensor $\sigma(t_n+\Delta t)$ using a given constitutive equation for the main program. If the calculated stress-strain results converge, then the main program continues the analysis at step t_{n+1}, and the next incremental step size is selected according to the convergence of the previous step. The accuracy of the Jacobi matrix or DDSDDE affects the convergence rate of the program but does not affect the accuracy of the results.

To better understand the collaborative work process of the ABAQUS main program and UMAT subroutine, taking the equivalent linear viscoelastic model used in this simulation as an example at an integral point of a material element, the detailed process is shown in Fig. 6.

In the UMAT subroutine of the numerical simulation, a user subroutine for the depicted viscoelastic model is provided in Fig. 7. The stress–strain relationship can be expressed as follows:

Table 1
Geometric parameters of the embankment model.

Parameter	Value
v_s (km/h)	108
h_1 (m)	3
h_e (m)	3
h_2 (m)	0.4
h_3 (m)	6
L (m)	20
L_1 (m)	10
L_2 (m)	19
L_3 (m)	35
M	1.5

Table 2
Parameters of the geogrid.

Project	Model	Rupture strength (kN/m)		Rupture elongation (%)		Width (m)
		Transverse	Longitudinal	Transverse	Longitudinal	
Geogrid	GG5050	≥50	≥50	≤4	≤4	13–20

Table 3
Parameters of the geocell.

Item	Unit	#1	#2	Method
Tensile yield strength	MPa	22	23	ASTM D638 (2010)
Flexural modulus	MPa	600	800	ASTM D638 (2010)
Impact strength	J/m	9	8	ASTM D256 (2010)
Normal temperature peel strength	kN/m	101	101	GB8808-88 (1988)

Table 4
Material parameters of each layer of embankment.

Layer	Density, ρ (kg/m^3)	Young Modulus, E (MPa)	Poisson's ratio, v	Angle of internal friction, φ (°)	Cohesion, c (kPa)
Pavement structure layer	2500	3000	0.2		
Embankment fill	1850	15	0.3	28	18
Gravel cushion layer	2100	30	0.25	30	0
Foundation soil	1800	10	0.3	25	20

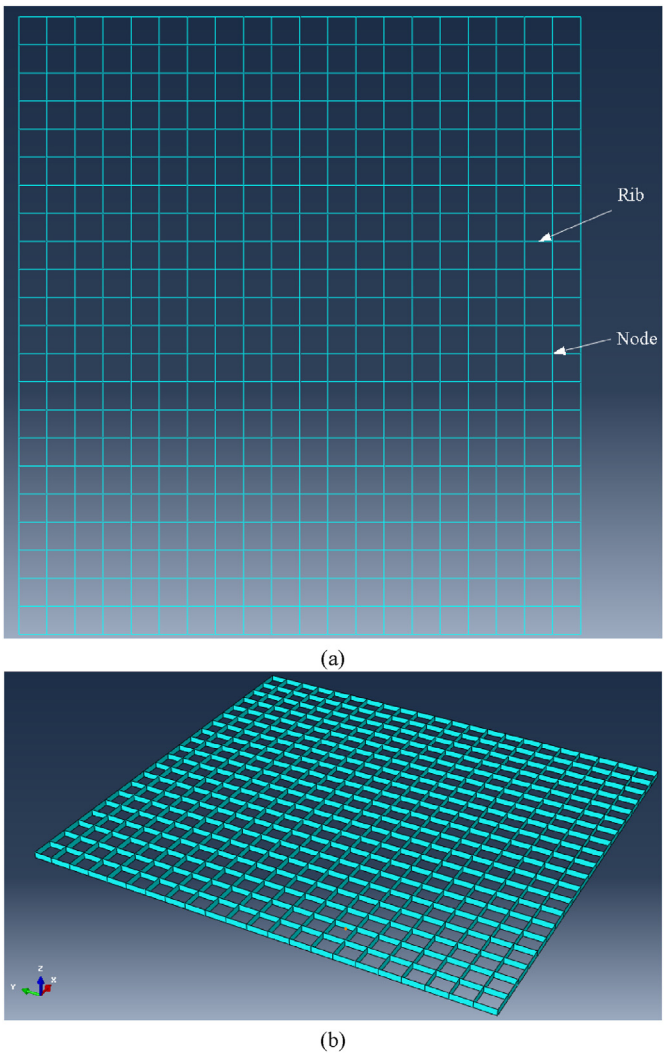

Fig. 5. Mesh of the reinforcement body: (a) Geogrid and (b) Geocell.

$$\sigma + \frac{\mu_1}{E_1 + E_2}\dot{\sigma} = \frac{\mu_1}{1 + E_1/E_2}\dot{\varepsilon} + \frac{1}{1/E_1 + 1/E_2}\varepsilon \tag{1}$$

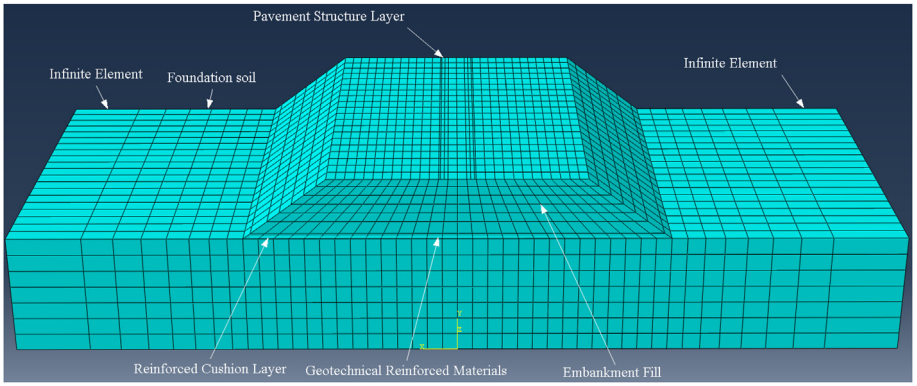

Fig. 4. Mesh generation of the geosynthetic-reinforced embankment.

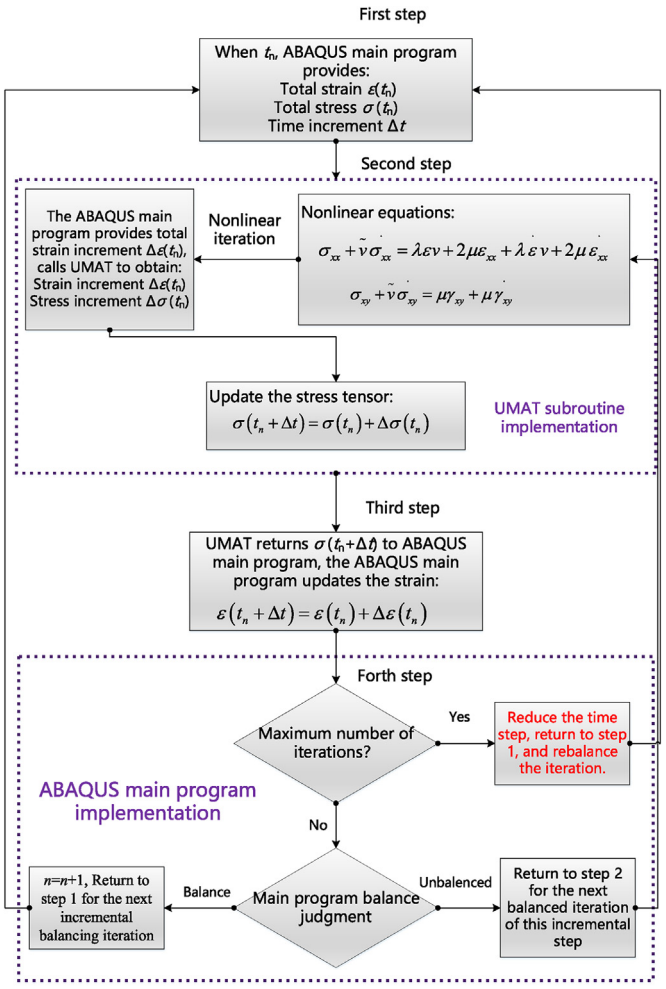

Fig. 6. Collaborative work process of the main program and UMAT subroutine.

where μ_1 is the coefficient of viscosity of the dashpot; E_1 is the Young's modulus of the spring that parallels with the dashpot; E_2 is the Young's modulus of the spring in series with the kelvin mode; ε, $\dot{\varepsilon}$ are the strain and the first derivative of the strain in the viscoelastic model, respectively; and σ, $\dot{\sigma}$ are the stress and the first derivative of the stress in the viscoelastic model, respectively. Note that the first derivative $\dot{\sigma}$ is a time-dependent variable.

The Young's modulus E_2 for the model shown in Fig. 7 is assumed to be infinite, and the model degenerates into the Kelvin model. In the actual calculation, E_2 equals $100E_1$, which can meet the requirements. The material used in the simulation contains five parameters, λ, μ, $\bar{\lambda}$, $\bar{\mu}$, and $\bar{\nu}$, where λ and μ are the Lame constants. Combining the viscoelastic model, μ should be determined by the dynamic shear modulus of the soil. If the Poisson's ratio is known, λ can also be determined. $\bar{\lambda}$ and $\bar{\mu}$ depend on the damping ratio. The two parameters are variables to establish the Jacobian matrix in the UMAT subroutine. According to Eq. (1), $\bar{\mu}$ is related to $\bar{\nu}$. Therefore, the subroutine code of the equivalent linear viscoelastic model for the soil can be obtained. The essential input in the viscoelastic model, i.e. the maximum dynamic shear modulus (G_{max}), will be controlled by the following four relevant variables, i.e. k, n, Poisson's ratio v, circular frequency w. These four parameters are model constants to calculate G_{max}. Also, another four state variables can be calculated via the developed subroutine, i.e. STATEV (1)-STATEV (4), which denote the confining pressure before earthquake, shear modulus ratio at a specific stress level, damping ratio, and maximum shear strain during earthquake, respectively. Then, we have

$$G_{max}=kp_a\left(\frac{\sigma_3'}{p_a}\right)^n \tag{2}$$

where p_a is the atmosphere pressure and σ_3' is the effective confining pressure (Xiao et al., 2023); k, n are the coefficients related to soil properties, including shape, gradation size, etc.

2.5. Moving load

The moving load was simulated by two rectangular patterns, and a Fortran subroutine was developed to control the amplitude, range, and speed of the moving load. The shape of the contact surface between the vehicle and the road is roughly an ellipse. However, owing to the complexity of the calculation of an ellipse load, it is generally simplified to a rectangle, and the load size is determined by the tire pressure. In this simulation, the load amplitude P is 100 kN (Zhang et al., 2020), the action range is represented by a rectangle with a length of 0.2 m and a width of 0.1 m (Cai et al., 2009; Qian et al., 2018), and the velocity of the moving load (v_s) is 108 km/h. The schematic diagram of the moving load is shown in Fig. 8.

2.6. Interaction

2.6.1. Model change

The model change allows elements to be killed and reactivated during the analysis, and it can be used for all the standard analytical steps. This study mainly used it to simulate the embankment filling process. It removes the specified elements from the model in the normal analysis step. Before the removal step, the standard analytical step stores the force applied by the removed region on the rest of the model on the node between them. During removal, these forces fall to zero. As a result, the impact of the removed area on the rest of the model disappears completely only at the end of the removal step. The force is gradually lowered to ensure that the removal of elements has a smooth effect on the model.

The stress/displacement elements (including structures) have two types of reactivation: no-strain reactivation and strain reactivation. This study uses the latter. For elements in the reactivation step, the implementation is as follows: let the displacement of the element node be the displacement shared by the rest of the model or the displacement specified by the boundary conditions. At any point in the activation step, a displacement is applied to the element as

$$u^e=\alpha(t)u^g \tag{3}$$

where u^e is displacement of any time, u^g is actual calculated displacement, and $\alpha(t)$ is a parameter that varies linearly from 0 to 1. Thus, in this step, the displacement of the reactivated elements gradually rises to their actual value.

2.6.2. Embedded region

The embedded element technique is used to specify that one group of elements are embedded into a host element. For example, the embedded region technology can be used for modeling the reinforcement. The numerical software searches for geometric relationships between nodes of the embedded elements and host elements. If the node of an embedded element is within the host element, the translational freedom of that node is eliminated and the node becomes an embedded node. The translational freedom of the embedded node is constrained by the interpolation within the

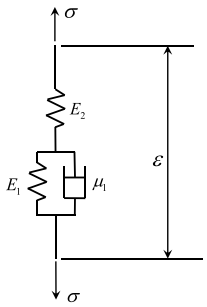

Fig. 7. Schematic diagram of the viscoelastic model.

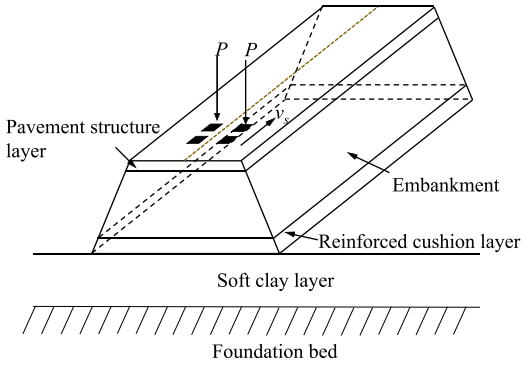

Fig. 8. Schematic diagram of moving load.

corresponding principal element freedom. The embedded elements are allowed for rotational degrees of freedom, but these rotations are not restricted by embedding. Multiple embedded element definitions are assumed. Many embedding models are used in 3D models: beam, membrane, shell, soil, surface, and truss embedding. This study mainly uses truss embedding and membrane embedding. More detailed information about the whole modeling procedures can be found in Fig. 9.

3. Validations for newly developed subroutine

To confirm the correctness and applicability of the developed Fortran subroutine in simulating the moving traffic loading, the displacements of the pavement structure layer under the moving load are compared between analytical solutions and numerical predictions in this study. Younesian et al. (2005) analyzed the ballastless track model using theoretical theorm and test data of an infinite beam on a viscoelastic foundation under a moving load. The physical and geometric parameters of the model are presented in Table 5. Here, the parameters obtained by Younesian et al. (2005) were used for numerical calculation. The calculation model of Younesian et al. (2005) is shown in Fig. 10. For the numerical calculation in this study, if the Young's modulus of the geosynthetic-reinforced cushion part of the embankment is increased by 100 times, it can be considered as a rigid foundation, and a calculation model close to that in Fig. 10 can be obtained approximately. The comparisons are shown in Fig. 11: the results represent the settlement schematic curve of the pavement structure layer at frequencies of 200 Hz, 300 Hz, and 400 Hz, respectively.

Younesian et al. (2005) did not consider the impact of the embankment fill weight and the interaction between the upper and lower parts in the theoretical solution process. However, the two

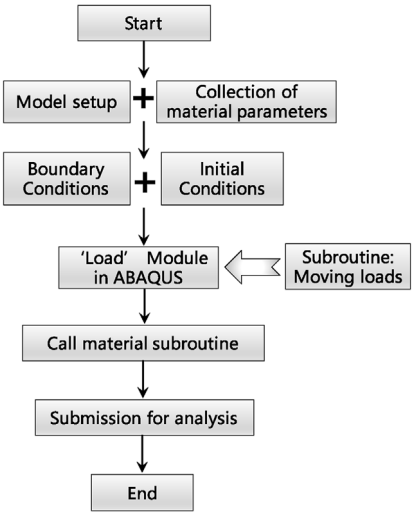

Fig. 9. Flowchart of numerical prediction for reinforced embankment performance in ABAQUS.

points were considered in Zhang et al. (2020)'s theory and the simulation in this study. In theory, the results of Zhang et al. (2020) are slightly larger than those of Younesian's study. When the frequency is 200 Hz, the displacements calculated by Zhang et al. (2020), Younesian et al. (2005), and the present study are 0.374 mm, 0.35 mm, and 0.340 mm, respectively. When the frequency is 300 Hz, the displacements calculated by Younesian et al. (2005) and the present study are 0.411 mm and 0.390 mm, respectively. At the frequency of 400 Hz, the displacements calculated by Younesian et al. (2005) and the present study are 0.256 mm and 0.241 mm, respectively. The numerical results in this study are slightly lower than Younesian's results. The reason may be that the foundation soil is considered as a continuum in the finite element analysis, and there is a mutual influence on the settlement and stress between each point. At the same time, it can also be found that there are obvious fluctuations near the load point in the numerical results, and the wave scenario increases as the frequency increases. This cannot be considered in the theoretical analysis.

In general, it can be observed from Fig. 11 that the numerical results in this study are basically consistent with the results of Younesian et al. (2005) and Zhang et al. (2020). This indicates that the proposed subroutine is capable of characterizing the moving features of traffic loads.

4. Spatial distribution characteristics of the pavement structure layer

The model size and calculation parameters are adopted based on the finite element numerical model of the geosynthetic-reinforced embankment under a moving load established in Section 2. The spatial characteristics of the dynamic response of geosynthetic-reinforced embankment under double moving loads are then investigated.

4.1. Spatial characteristics of dynamic stress

Fig. 12a–h shows the spatial distribution of stress in the pavement structure layer when the moving load (P = 100 kN) moves longitudinally along the geosynthetic-reinforced embankment at the velocity v_s = 108 km/h. In Fig. 12, σ_v is the vertical stress due to

Table 5
Properties of the rail, foundation and load.

Item	Property	Symbol	Value
Rail (UIC60)	Young's modulus of the track	E_T	210 GPa
	Shear modulus of the track	G	77 GPa
	Mass density	ρ	7850 kg/m^3
	Cross-sectional area	A	7.69 × 10^{-3} m^2
	Moment of area	I	30.55 × 10^{-6} m^4
	Shear coefficient	k^*	0.4
Foundation	Mean stiffness	k_m	202.33 MN/m^2
	Mean loss factor	η_m	0.58
	Coefficient of variation of stiffness	σ_{km}	1.756 × 10^{15} m^4
	Loss of coefficient of variation	$\sigma_{\eta m}$	0.073
Moving load	Load	F	65 kN

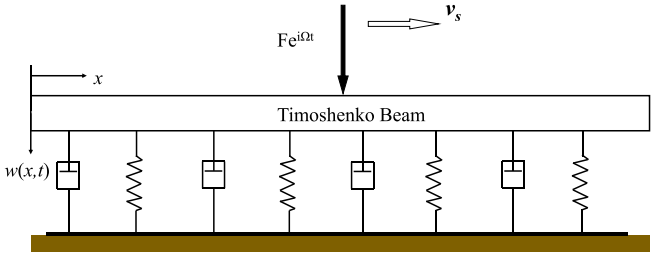

Fig. 10. Younesian's model (after Younesian et al., 2005).

the moving loads, S_1 is the distance from the embankment centerline, S_2 is the longitudinal distance along the embankment, and t is the duration for the traffic loading motion.

As seen from Fig. 12a–h, the amplitude of the vertical stress is approximately 20 kPa. When the load moves from the left (t = 0.051 s) to the right (t = 0.612 s) on the reinforced embankment, the change in the stress of the pavement structure layer is mainly obvious near the load area. In the transverse direction at any time, a trend of a large stress in the middle and a small stress on both sides can be observed.

4.2. Spatial characteristics of dynamic strain

The spatial distribution of displacement for the pavement structure layer when the moving load (P = 100 kN) moves on the geosynthetic-reinforced embankment at the velocity v_s = 108 km/h is presented in Fig. 13a–h. The maximum vertical displacement under the self-weight of the embankment fill is 7.1 mm. Due to the moving load, the maximum displacement amplitude is approximately 7.15 mm. As observed from Fig. 13a–h, the vertical displacement of the pavement structure layer caused by the moving load is mainly concentrated near the load area, and it advances in the direction of the load movement in a conical shape. In addition, there is an obvious local "convex" or "concave" scenario near the load point along the direction of the load movement.

5. Parametric study

A parametric study was carried out to investigate the response of the geosynthetic-reinforced embankment system by varying the reinforcement type, overload, velocity of the moving load (v_s), height of the embankment fill (h_e), and stiffness of the pavement structure layer. The basic calculation parameters used in the parametric study are listed in Tables 1–4

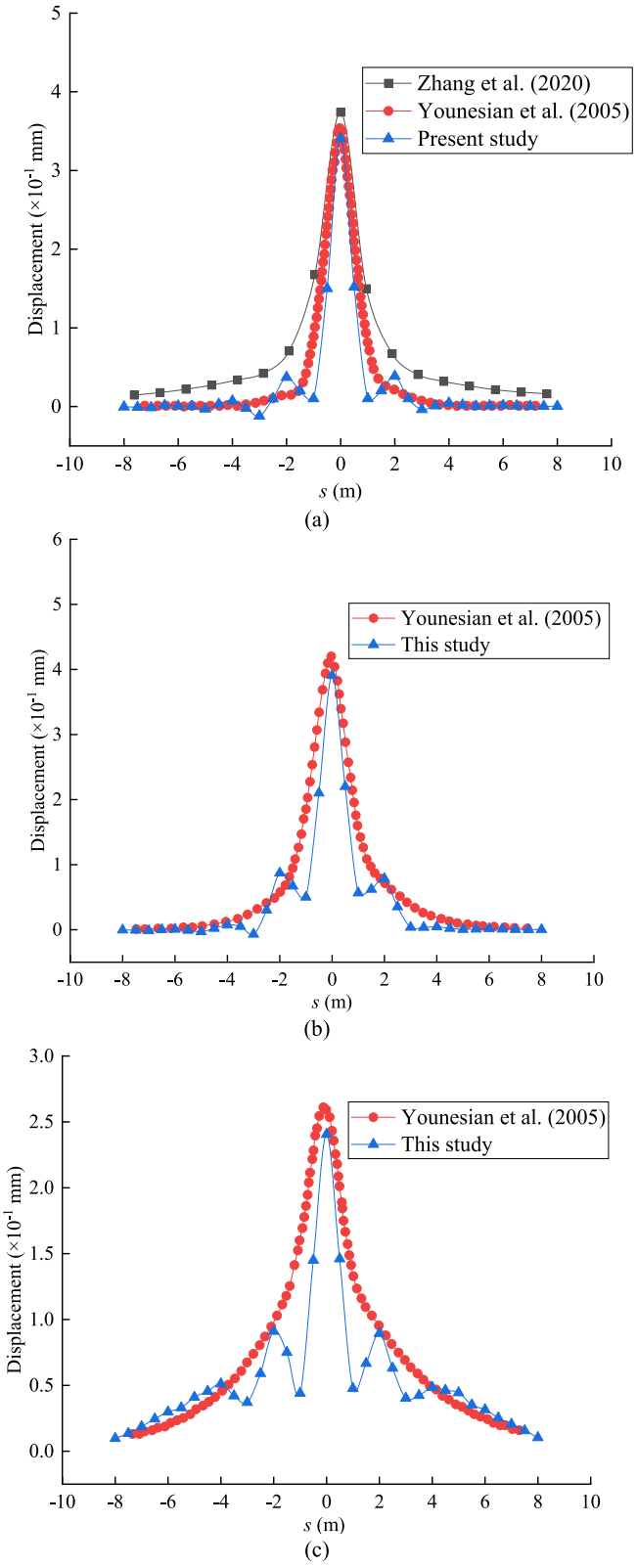

Fig. 11. Comparison between the present study, Younesian et al. (2005)'s and Zhang et al. (2020)'s study: (a) f = 200 Hz, (b) f = 300 Hz, and (c) f = 400 Hz.

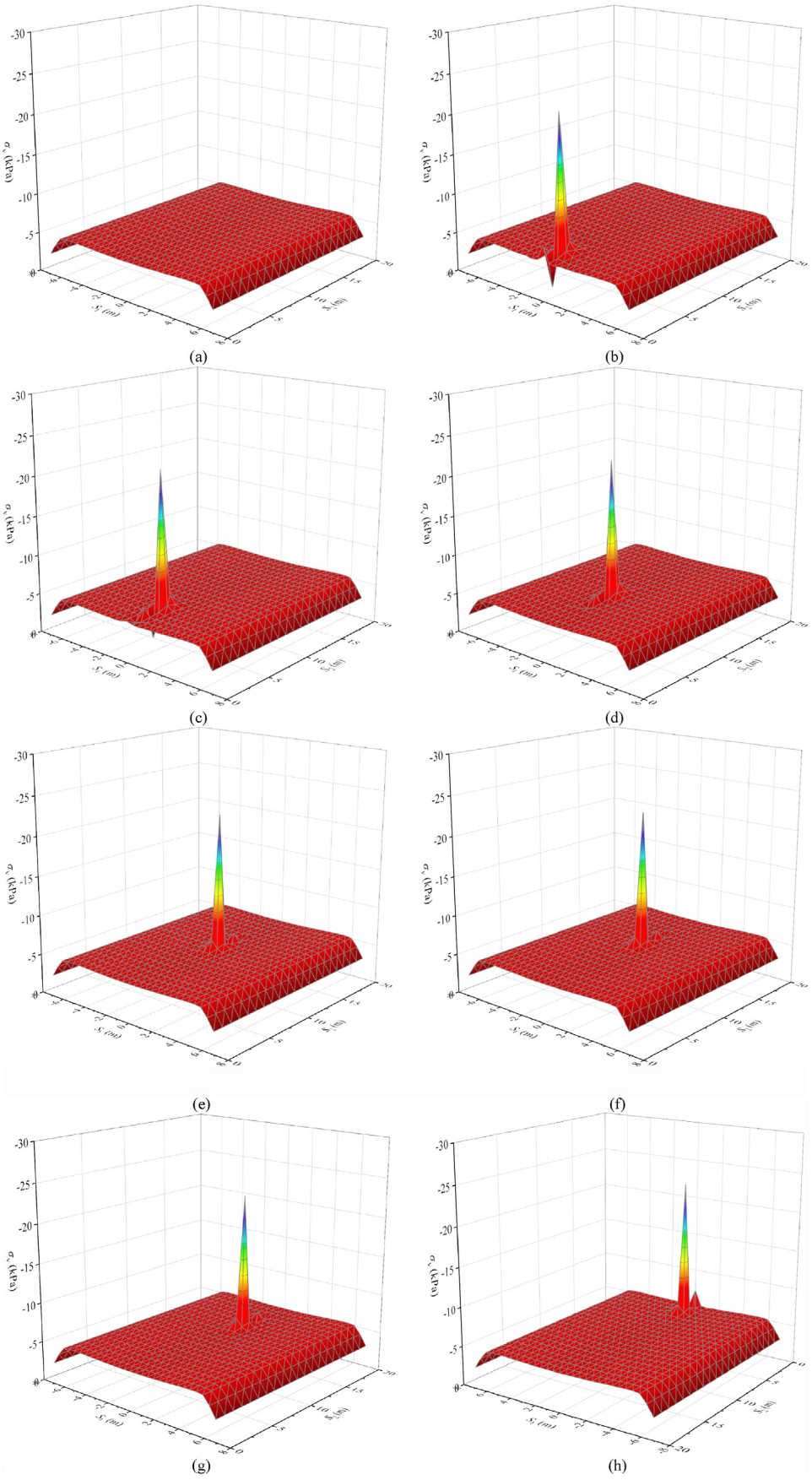

Fig. 12. Spatial distribution of stress in the pavement structure layer: (a) $t = 0.051$ s, (b) $t = 0.068$ s, (c) $t = 0.136$ s, (d) $t = 0.272$ s, (e) $t = 0.357$ s, (f) $t = 0.391$ s, (g) $t = 0.459$ s, and (h) $t = 0.612$ s.

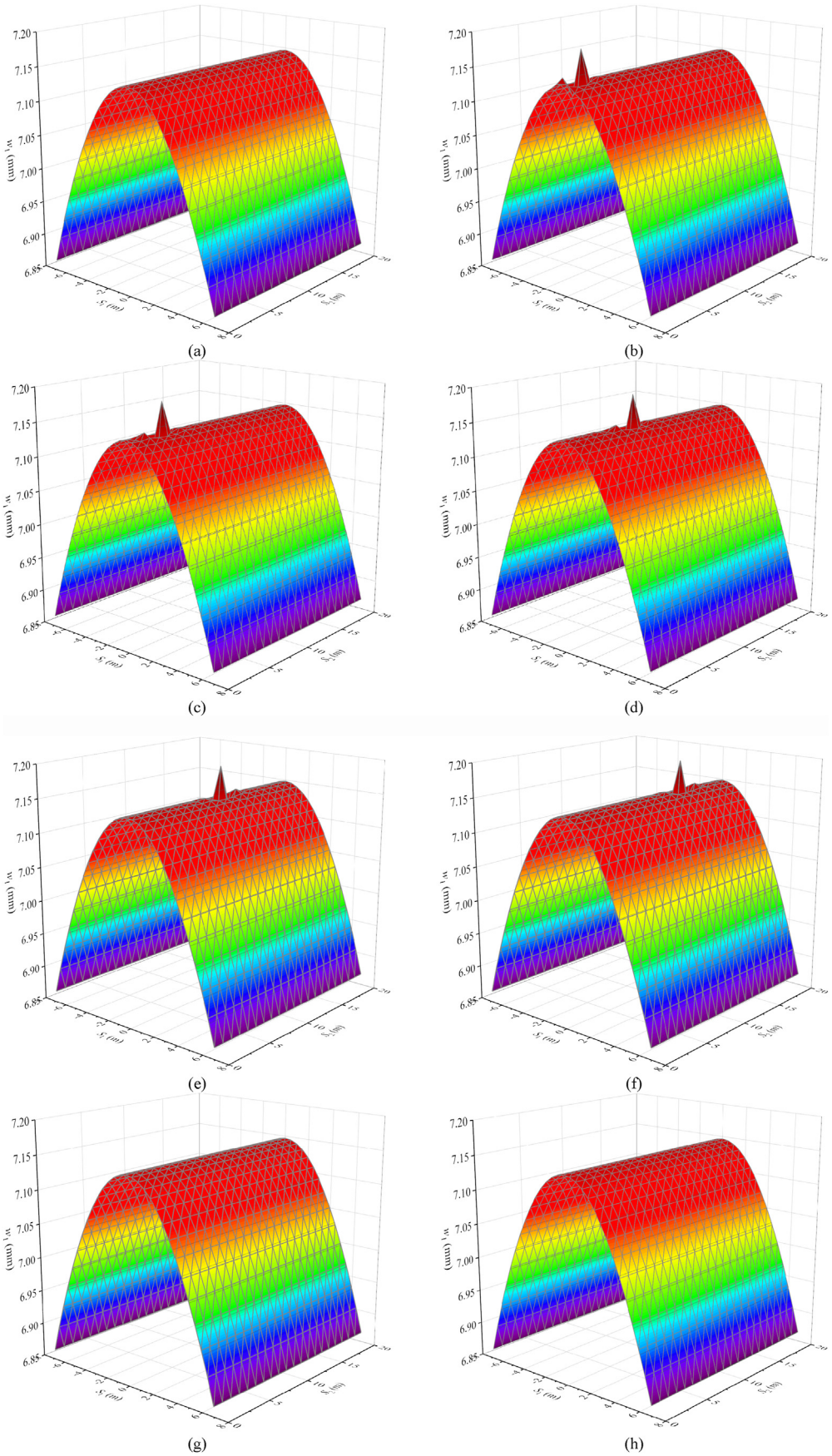

Fig. 13. Spatial distribution of displacement in the pavement structure layer: (a) $t = 0.051$ s, (b) $t = 0.068$ s, (c) $t = 0.136$ s, (d) $t = 0.272$ s, (e) $t = 0.357$ s, (f) $t = 0.391$ s, (g) $t = 0.459$ s, and (h) $t = 0.612$ s.

5.1. Reinforcement type

This section mainly studies the dynamic response of the embankment with different types of geosynthetic reinforcement (geogrid or geocell) under the moving loads. Fig. 14 depicts the longitudinal deformation of the pavement structure layer with different reinforcement types. The deformation trend of the pavement structure layer is roughly the same when the reinforcement is geogrid or geocell, as observed in Fig. 14, where w_1 is the vertical deformation of the pavement structure layer. The difference is that the maximum value and the overall deformation of the pavement structure layer are reduced when the reinforcement is the geocell compared to those with a geogrid. This is due to the 3D structure of the geocell, where the reinforced cushion layer forms a whole with greater flexural rigidity that decreases the deformation of the entire pavement structure layer. Fig. 15 shows the deformation of the surface of the reinforced cushion layer. Similar rules hold, and the deformation of the reinforced cushion layer is much smaller than that of the pavement structure layer, as can be observed in Fig. 15, where w_2 is the vertical deformation of the reinforced cushion layer.

Fig. 16 shows the stress distribution in the cross-section of the pavement structure layer, where σ_{v1} is the vertical stress of this layer. The maximum stress is reduced by 28.7% as it decreases from 27.68 kPa to 19.75 kPa while the distribution of the stress is kept unchanged. Fig. 17 shows the stress distribution at the surface of the reinforced cushion layer with different reinforcement types, where σ_{v2} is the vertical stress of the reinforced cushion layer. There is a small stress fluctuation on the surface of the reinforced cushion layer. The main reason for the fluctuation of the dynamic stress is that the reinforced cushion and the upper and lower soil are divided into two parts, and the nodes and elements of each part are balanced. The calculation results of the upper and lower interfaces of the reinforced cushion are the nodes of the contact interface, and the nodes at the interface belong to two entireties. There will induce slightly unequal stress and deformation, resulting in the stress fluctuation. In addition, the surface stress of the geocell cushion layer is slightly less than that of the geogrid cushion layer, and the scenario of fluctuation on the surface of the reinforced cushion layer is sound when using the geocell. This may be due to the increased stiffness of the cushion layer.

Figs. 18 and 19 present the tensile stress distribution of the reinforcement body with different types of reinforcements, where T_R is the tensile stress of the reinforcement body. Because the tensile stress of the geogrid is only in one direction, this is a

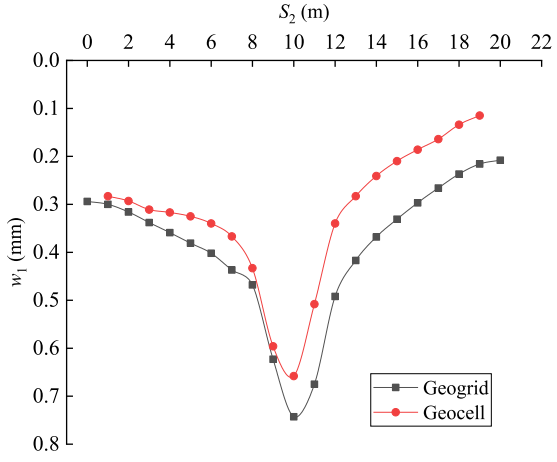

Fig. 14. Longitudinal deformation of the pavement structure layer.

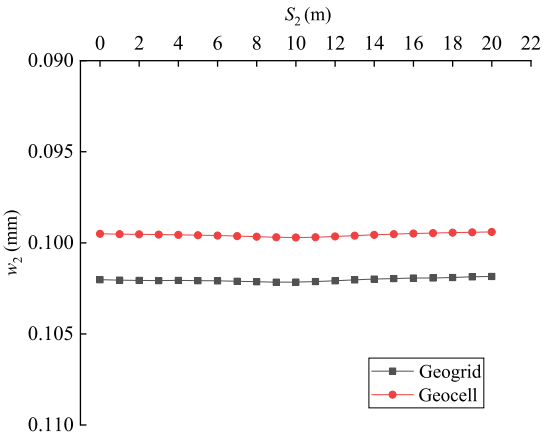

Fig. 15. Longitudinal deformation of the reinforced cushion layer.

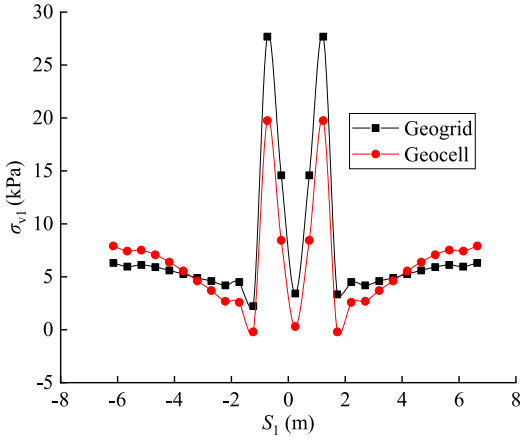

Fig. 16. Stress distribution in the cross-section of the pavement structure layer.

"convex" type, i.e. the tensile stress in the middle of the geogrid is large, and the tensile stress at both ends is relatively small. As the geocell reinforcement is a 3D structure, the tensile stresses in the reinforcement are divided into two directions, including the horizontal and vertical stresses. The vertical load will be converted into horizontal load through the geocell reinforcement, and the horizontal and vertical tensions show an obvious "step-like" pattern. Fig. 20 shows the deformation of the reinforced body of the geogrid and geocell. It is evident from Fig. 20 that the trend of the deformation for the reinforced body is basically consistent with different types of reinforcements. The deformation of the reinforced body is slightly smaller when using the geocell-reinforcement than that using the geogrid, with a reduction of approximately 18.5%.

From the above analysis, it can be observed that compared with the geogrid-reinforced embankment, the use of geocell can reduce the deformation of the pavement structure layer more obviously under the same moving loads. It also improves the stress distribution of the pavement structure layer and the reinforced cushion layer. In addition, it increases the tensile force of the reinforcement material. This plays an important role in improving the bearing capacity of the reinforced embankment.

5.2. Overload

As vehicle overload is a common problem in highway engineering, a sensitivity analysis of the vehicle overload in geosynthetic-reinforced embankment systems was performed.

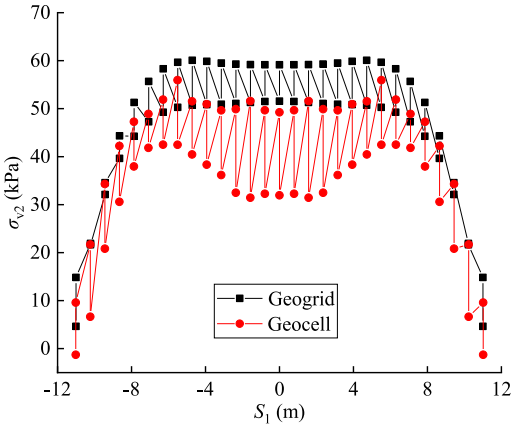

Fig. 17. Stress distribution in cross-section of the reinforced cushion layer.

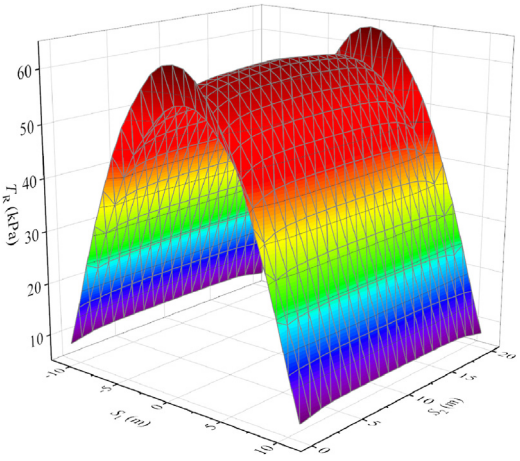

Fig. 18. Geogrid tension.

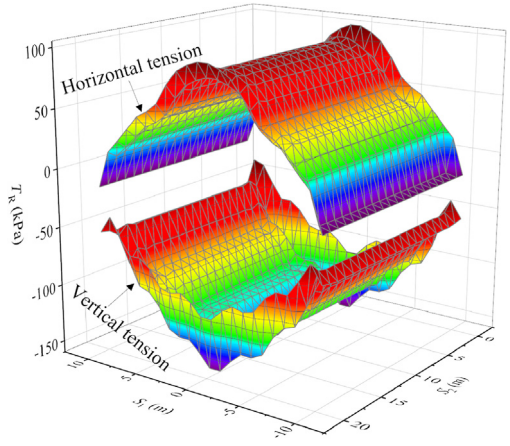

Fig. 19. Geocell tension.

Fig. 21 shows the stress distribution of the pavement structure layer in the cross-section when the load changes from normal load (P = 100 kN), to 30% overload (P = 130 kN), 50% overload (P = 150 kN), 100% overload (P = 200 kN), 200% overload (P = 300 kN), respectively, where σ_v is the vertical stress. It is found from Fig. 21 that because there are two moving loads on the cross-section, the corresponding cross-section stress distribution has two wave peaks, while the stress on both sides of the load is smaller. Moreover, it can be observed that the stress curve fluctuations may occur on both sides of the maximum local stress, and the overall stress amplitude increases gradually with increase in the overload.

As observed from Fig. 22, where w_1 is the deformation of the pavement structure layer, with the increase in moving load overload, the deformation of the entire pavement structure layer showed an increasing trend, and the change in vertical deflection is particularly evident within a scope of 4 m under the moving load. Compared with the normal load (P = 100 kN), the maximum vertical deflection increased 4.2% with 30% overload, 14.6% with 50% overload, 34.3% with 100% overload, and 55.3% with 200% overload. The local deformation of the loading range obviously increases under the overload. Fig. 23 displays the relationship between the attenuation coefficient and overload. Here, the attenuation coefficient of the deformation is α_u, whose value is equal to the ratio of the vertical deformation of the reinforced cushion layer to the vertical deformation of the pavement structure layer. The attenuation coefficient of the stress is α_s, which is equal to the ratio of the vertical stress increment of the reinforced cushion layer to that of the pavement structure layer. From Fig. 23, it can be observed that α_u decreases gradually with increase in the overload. When the load increased from the normal load to 200% overload, α_u decreased from 10.57% to 6.85% with a small change. At the same time, the attenuation coefficient of stress (α_s) also decreased with the increase in overload, but the decreased amplitude is relatively larger.

5.3. Velocity of moving load

Figs. 24–28 show the deformation, stress, and variation of the tensile force of the reinforcement material of the pavement structure layer, the reinforced cushion layer, and the reinforcement body under the different vehicle speeds. Only highway traffic loads are considered here. Thus, the velocity v_s is, respectively, 30 km/h, 60 km/h, 90 km/h, 120 km/h, 150 km/h and 180 km/h. The remaining parameters are the same as those in previous sections.

Fig. 24 shows the deformation in the longitudinal section of the pavement structure layer under different moving speeds. The load moves from the left to right, showing an asymmetric deformation distribution where the deformation after the action of the load is slightly larger than that before the action of the load, and the local deformation below the load attains the maximum value. When the moving velocity of the load increases from 30 km/h to 180 km/h, the deformation of the longitudinal section increases gradually. Especially at velocity v larger than 120 km/h, the increase in the

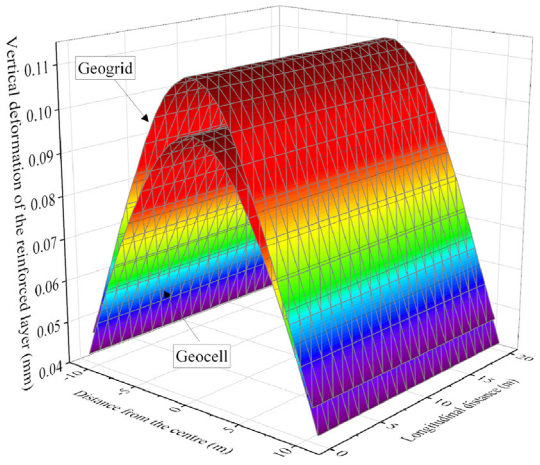

Fig. 20. Deformation with different reinforced types.

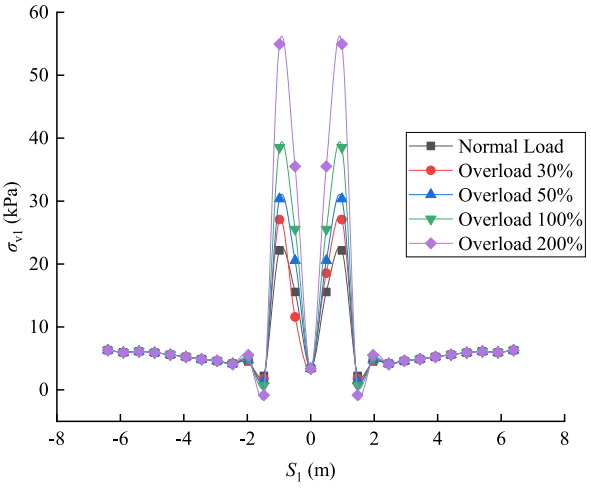

Fig. 21. Vertical stress of the pavement structure layer.

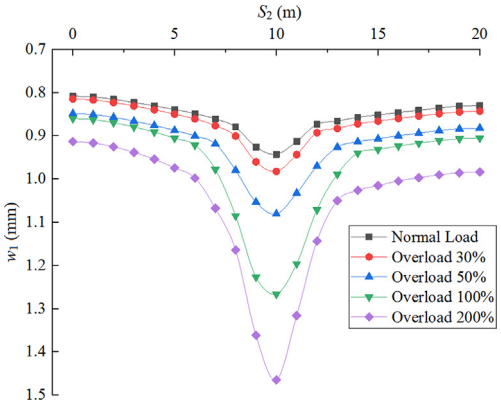

Fig. 22. Vertical displacement of the longitudinal section of the pavement structure layer.

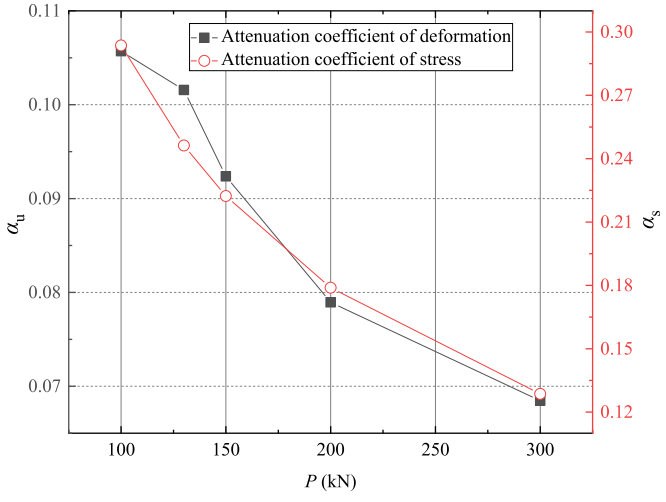

Fig. 23. Relationship between α_u, α_s, and overload.

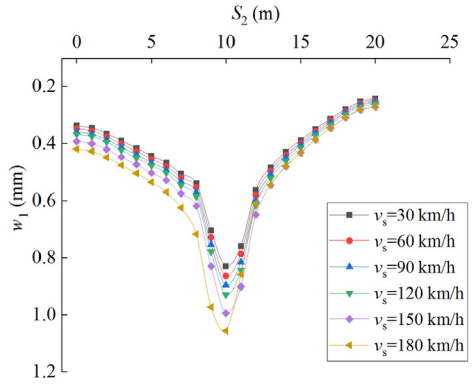

Fig. 24. Deformation in the longitudinal section of the pavement structure layer.

vertical deformation will be intensified. For example, in Fig. 25, the maximum deformation increases from 0.83 mm to 0.896 mm, an increase of 8%, when the velocity increases from 30 km/h to 90 km/h, while the maximum deformation increases from 0.928 mm to 1.056 mm, an increase of 13.8%, when the velocity increases from 120 km/h to 180 km/h. However, the deformation of the reinforced cushion layer is not sensitive to the variation in the moving load velocity. $w_{1,max}$ and $w_{2,max}$ in Fig. 25 are the maximum vertical deformations of the pavement structure layer and the reinforced cushion layer, respectively. Fig. 26 shows the stress distribution of the cross-section of the pavement structure layer, and an increase in the speed of the moving load will increase the stress of the pavement structure layer, especially at the load position. In Fig. 27, $\sigma_{v1,max}$ and $\sigma_{v2,max}$ are the maximum vertical stresses of the pavement structure layer and the reinforced cushion layer, respectively. The stress of the reinforced cushion layer will also increase, but the increase is significantly less than that of the pavement structure layer. When the velocity of the moving load increases from 30 km/h to 180 km/h, the stress of the pavement structure layer increases from 19.69 kPa to 25.43 kPa by 29.3%. The stress of the reinforced cushion layer increases from 5.75 kPa to 6.51 kPa by 13.3%.

Fig. 28 shows the variation in the deformation attenuation coefficient (α_u) and stress attenuation coefficient (α_s) with velocity v. As can be observed in Fig. 28, both the attenuation coefficients of deformation and the stress decrease with increase in the velocity. The reason may be that when the speed of the moving load is high, the vibration of the reinforced embankment mainly occurs at the surface of the embankment structure and the deformation and stress of the pavement structure layer will increase, thus increasing the denominator of the attenuation coefficient and decreasing the attenuation coefficient. Meanwhile, it can also be observed that the attenuation degree of stress is greater than the attenuation degree of deformation. When the velocity increases from 30 km/h to 210 km/h, the attenuation coefficient of deformation (α_u) decreases from 12% to 8.87%, and the attenuation coefficient of stress (α_s) decreases from 29.2% to 24.96%.

6. Conclusions

A numerical model was proposed for investigating a geosynthetic-reinforced embankment on an elastic foundation under a traffic load moving at a constant velocity. The pavement structure was idealized as an elastic plate, and the geosynthetic-reinforced granular mattress was investigated by the geotechnical

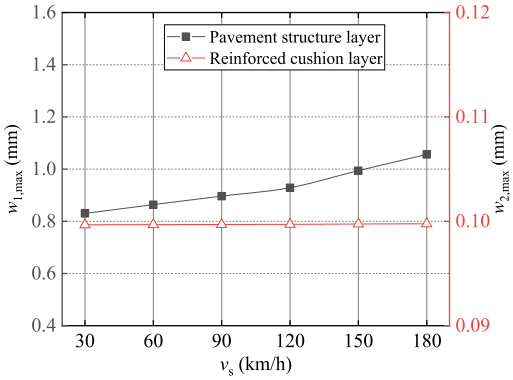

Fig. 25. Maximum deformation of the pavement structure layer and reinforced cushion layer.

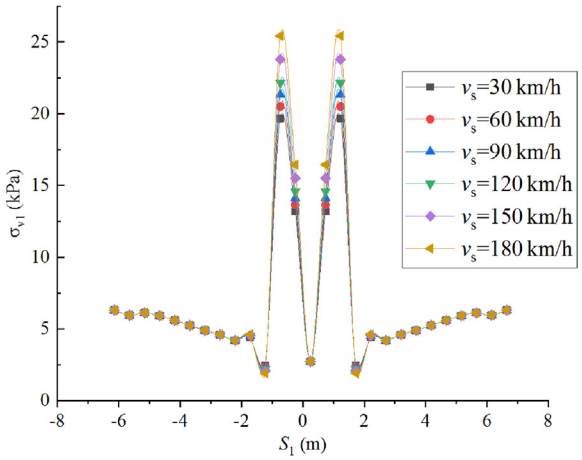

Fig. 26. Stress in the cross-section of the pavement structure layer.

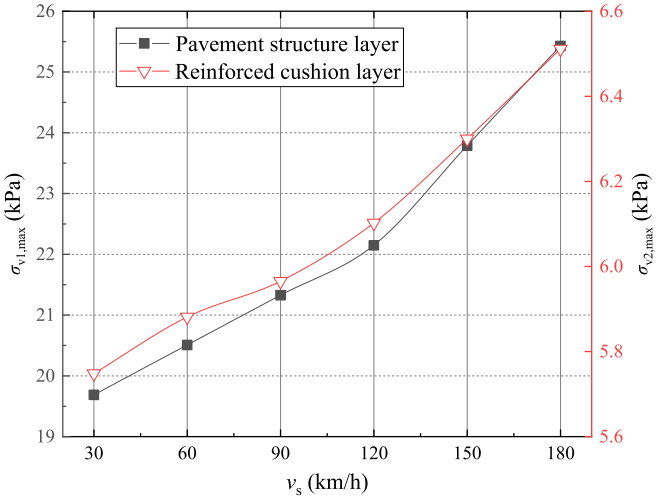

Fig. 27. Maximum stress in the pavement structure layer and reinforced cushion layer.

material with different bending stiffnesses. The upper and lower soil layers were idealized as viscoelastic soil with different

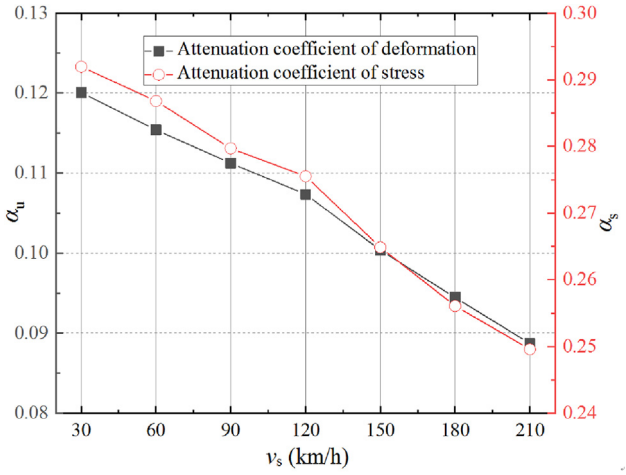

Fig. 28. Relationship between α_u, α_s and v_s.

stiffnesses and viscous damping. By means of parametric study, the geosynthetic-reinforced embankment performance was analyzed. The main findings of this study can be summarized as follows:

(1) The numerical model of the geosynthetic-reinforced embankment under moving loads was established by a secondly-developed Fortran subroutine in ABAQUS in the framework of the infinite elements. The traffic loads were simulated by two moving loads of rectangular pattern. Considering the viscoelasticity of the embankment fill, the equivalent linear viscoelasticity model was developed by the ABAQUS user material subroutine to investigate the deformation of the embankment fill.

(2) Compared with the geogrid-reinforced embankment, the use of geocell can reduce the deformation of the pavement structure layer significantly under the same moving loads. Moreover, it can also improve the stress distributions of the pavement structure layer and the reinforced cushion layer with increased tension within the geo-reinforcement.

(3) Overloaded vehicles are frequently encountered in highway engineering. With the increase in overload, the stress and deformation of the pavement structure will increase significantly, especially when the overload surpasses 50%. Additionally, higher velocity significantly affects the vertical displacement as well as the stress of the geosynthetic-reinforced embankment, and thus, the velocity of the traffic load should be under control, e.g. less than 120 km/h.

Declaration of competing interest

The authors declare that they have no known competing financial interests or personal relationships that could have appeared to influence the work reported in this paper.

Acknowledgments

This research was funded through the National Natural Science Foundation of China (Grant Nos. 52108299 and 52178312), the China Postdoctoral Science Foundation (Grant No. 2021M693740), and the Basal Research Fund Support by Chongqing University.

List of notations

A	Cross-sectional area
c	Cohesion
E	Young's modulus of the soil layer
E_T	Young's modulus of the track
f	Frequency of the moving load
G	Shear modulus of the track
h_1	Height of the pavement structure layer
h_e	Effective height of embankment filling
h_2	Height of the reinforced cushion layer
h_3	Height of the substratum of the foundation
I	Moment of area
k^*	Shear coefficient
k_m	Mean stiffness
L	Length in longitudinal direction
L_1	Width of the pavement structure layer
L_2	Width at the bottom of the geosynthetic-reinforced embankment
L_3	Width of the foundation soil
m	Slope ratio of the reinforced embankment
P	Amplitude of the moving load
s	Distance
S_1	Distance from the center
S_2	Longitudinal distance along the embankment
t	Time
T_R	Tension of the reinforcement body
U_1	Horizontal displacement
U_2	Horizontal displacement
v_s	Speed of the moving load
$w(x, t)$	Displacement of the Timoshenko beam
w_1	Displacement of the pavement structure layer
w_2	Displacement of the reinforced cushion layer
$w_{1,max}$	Maximum displacement of the pavement structure layer
$w_{2,max}$	Maximum displacement of the reinforced cushion layer
γ_e	Effective weight of the embankment filling
ρ	Mass density
μ	Poisson's ratio
φ	Angle of internal friction
η_m	Mean loss factor
σ_{km}	Coefficient of variation of stiffness
$\sigma_{\eta m}$	Loss of coefficient of variation
σ_v	Vertical stress
σ_{v1}	Vertical stress of the pavement structure layer
σ_{v2}	Vertical stress of the reinforced cushion layer
$\sigma_{v1,max}$	Maximum vertical stress of the pavement structure layer
$\sigma_{v2,max}$	Maximum vertical stress of the reinforced cushion layer
α_u	Attenuation coefficient of deformation
α_S	Attenuation coefficient of stress

References

Abdullah, C.H., Edil, T.B., 2007. Behaviour of geogrid-reinforced load transfer platforms for embankment on rammed aggregate piers. Geosynth. Int. 14 (3), 141–153.

ASTM D638, 2010. Standard Test Method for Tensile Properties of plastics. West Conshohocken, PA, USA.

ASTM D256, 2010. Standard test method for determining the load pendulum impact resistance of plastics. West Conshohocken, PA, USA.

Biabani, M.M., Indraratna, B., Ngo, N.T., 2016. Modelling of geocell-reinforced subballast subjected to cyclic loading. Geotext. Geomembranes 44 (4), 489–503.

Biswas, A., Krishna, A.M., Dash, S.K., 2016. Behavior of geosynthetic reinforced soil foundation systems supported on stiff clay subgrade. Int. J. GeoMech. 16 (5), 04016007.

Bourgeois, E., Soyez, L., Le, Kouby A., 2011. Experimental and numerical study of the behavior of a reinforced-earth wall subjected to a local load. Comput. Geotech. 38 (4), 515–525.

Cai, Y.Q., Gao, Z.G., Sun, H.L., Xu, C.J., 2009. Dynamic response of pavements on poroelastic half-space soil medium to a moving traffic load. Comput. Geotech. 36, 52–60.

Chen, J., Zhou, Y., 2018. Dynamic responses of subgrade under double-line high-speed railway. Soil Dynam. Earthq. Eng. 110, 1–12.

Dash, S.K., 2003. Model studies on circular footing supported on geocell-reinforced sand underlain by soft clay. Geotext. Geomembranes 21 (4), 197–219.

Dash, S.K., 2012. Effect of geocell type on load-carrying mechanisms of geocell-reinforced sand foundations. Int. J. GeoMech. 12 (5), 537–548.

Dash, S.K., Bora, M.C., 2013. Improved performance of soft clay foundations using stone columns and geocell-sand mattress. Geotext. Geomembranes 41, 26–35.

Deb, K., Basudhar, P.K., Chandra, S., 2007. Generalized model for geosynthetic-reinforced granular fill-soft soil with stone columns. Int. J. GeoMech. 7 (4), 266–276.

Deb, K., Samadhiya, N.K., Namdeo, J.B., 2011. Laboratory model studies on unreinforced and geogrid-reinforced sand bed over stone column-improved soft clay. Geotext. Geomembranes 29 (2), 190–196.

Dutta, S., Mandal, J.N., 2016. Model studies on geocell-reinforced fly ash bed overlying soft clay. J. Mater. Civ. Eng. 28 (2), 04015091.

Fakher, A., Jones, C.J.F.P., 2001. When the bending stiffness of geosynthetic reinforcement is important. Geosynth. Int. 8 (5), 445–460.

GB8808-88, 1988. Test method for peel force of flexible laminated plastics.

Han, J., Gabr, M.A., 2002. Numerical analysis of geosynthetic-reinforced and pile-supported earth platforms over soft soil. J. Geotech. Geoenviron. Eng. 128 (1), 44–53.

Hegde, A., Sitharam, T.G., 2015. 3-Dimensional numerical modelling of geocell reinforced sand beds. Geotext. Geomembranes 43 (2), 171–181.

Hong, Y.S., Wu, C.S., 2013. The performance of a sand column internally reinforced with horizontal reinforcement layers. Geotext. Geomembranes 41, 36–49.

Huang, J., Parsons, R.L., Han, J., Pierson, M., 2011. Numerical analysis of a laterally loaded shaft constructed within an MSE wall. Geotext. Geomembranes 29 (3), 233–241.

Indraratna, B., Biabani, M.M., Nimbalkar, S., 2015. Behavior of geocell-reinforced subballast subjected to cyclic loading in plane-strain condition. J. Geotech. Geoenviron. Eng. 141 (1), 04014081.

Leshchinsky, B., Ling, H., 2013. Effects of geocell confinement on strength and deformation behavior of gravel. J. Geotech. Geoenviron. Eng. 139 (2), 340–352.

Liu, S.L., Wang, L.Q., Zhang, W.G., He, Y.W., Pijush, S., 2023. A comprehensive review of machine learning-based methods in landslide susceptibility mapping. Geol. J. https://doi.org/10.1002/gj.4666.

Maheshwari, P., Chandra, S., Basudhar, P.K., 2004. Response of beams on a tensionless extensible geosynthetic-reinforced earth bed subjected to moving loads. Comput. Geotech. 31 (7), 537–548.

Ngo, N.T., Indraratna, B., Rujikiatkamjorn, C., Biabani, M.M., 2016. Experimental and discrete element modeling of geocell-stabilized subballast subjected to cyclic loading. J. Geotech. Geoenviron. Eng. 142 (4), 04015100.

Peng, Y., Liu, H.L., Li, C., et al., 2021. The detailed particle breakage around the pile in coral sand. Acta Geotech. https://doi.org/10.1007/s11440-020-01089-2.

Pham, H.V., Dias, D., 2019. 3D numerical modeling of a piled embankment under cyclic loading. Int. J. GeoMech. 19 (4), 04019010.

Qian, Y., Mishra, D., Tutumluer, E., Kazmee, H.A., 2015. Characterization of geogrid reinforced ballast behavior at different levels of degradation through triaxial shear strength test and discrete element modeling. Geotext. Geomembranes 43 (5), 393–402.

Qian, J.G., Zhou, R.Y., Chen, S.L., Gu, X.Q., Huang, M.S., 2018. Influence of pavement roughness on dynamic stresses in saturated subsoil subjected to moving traffic loading. Int. J. GeoMech. 18 (4), 04018012.

Shadi, A., Shukla, S.K., Mohyeddin, A., 2019. Numerical investigation of wraparound geotextile reinforcement technique for strengthening foundation soil. Int. J. GeoMech. 19 (4), 04019003.

Shi, J.W., Wang, Y., Ng, C.W.W., 2016. Numerical parametric study of tunneling-induced joint rotation angle in jointed pipelines. Can. Geotech. J. 53 (12), 2058–2071.

Suku, L., Prabhu, S.S., Ramesh, P., Babu, G.L.S., 2016. Behavior of geocell-reinforced granular base under repeated loading. Transp. Geotech. 9, 17–30.

Tang, X.C., Stoffels, S.M., Palomino, A.M., 2016. Mechanistic-empirical approach to characterizing permanent deformation of reinforced soft soil subgrade. Geotext. Geomembranes 44 (3), 429–441.

Thach, P.N., Liu, H.L., Kong, G.Q., 2013. Vibration analysis of pile-supported embankments under high-speed train passage. Soil Dyn. Earthq. Eng. 55, 92–99.

Thakur, J.K., Han, J., Parsons, R.L., 2017. Factors influencing deformations of geocell-reinforced recycled asphalt pavement bases under cyclic loading. J. Mater. Civ. Eng. 29 (3), 04016240.

Xiao, Y., Li, H.Y., Shi, J.Q., et al., 2023. Effect of particle size on small strain stiffness of biotreated sands. Transp. Geotech. 41, 101027.

Younesian, D., Kargarnovin, M.H., Thompson, D.J., Jones, C.J.C., 2005. Parametrically excited vibration of a Timoshenko beam on random viscoelastic foundation subjected to a harmonic moving load. Nonlinear Dynam. 45 (1–2), 75–93.

Zhang, L., Zhao, M.H., Shi, C.J., Zhao, H., 2010. Bearing capacity of geocell reinforcement in embankment engineering. Geotext. Geomembranes 28 (5), 475–482.

Zhang, L., Ou, Q., Zhao, M.H., 2018. Double-beam model to analyze the performance of a pavement structure on geocell-reinforced embankment. J. Eng. Mech. 144 (8), 06018002.

Zhang, L., Ou, Q., Zhou, S., 2020. Analytical study of the dynamic response of a double-beam model for a geosynthetic-reinforced embankment under traffic loads. Comput. Geotech. 118, 103330.
Zhang, K.Q., Wang, L.Q., Dai, Z.W., Huang, B.L., Zhang, Z.H., 2022. Evolution trend of the Huangyanwo rock mass under the action of reservoir water fluctuation. Nat. Hazards. https://doi.org/10.1007/s11069-022-05359-y.
Zhuang, Y., Cheng, X., Wang, K., 2020. Analytical solution for geogrid-reinforced piled embankments under traffic loads. Geosynth. Int. 27 (3), 249–260.
Zhuang, Y., Hu, S.L., Song, X.W., Zhang, H.R., Chen, W., 2022. Membrane effect of geogrid reinforcement for low highway piled embankment under moving vehicle loads. Sysmetry-Basel. 14 (10), 2162. https://doi.org/10.3390/sym14102162.
Zhou, H., Kong, G.Q., Liu, H.L., Laloui, L., 2018. Similarity solution for cavity expansion in thermoplastic soil. Int. J. Numer. Anal. Model. 42 (2), 274–296.

Dr. Xuanming Ding is engaged in pile foundation dynamics, soft soil foundation reinforcement theory and technology research. He has published 141 papers, one academic monographs. He also participated in the compilation of four national and industry standards and two provincial and ministerial regulations.